Hard X-ray Resonant Techniques for Studies of Nanomagnetism

George Srajer, Jonathan C. Lang and Daniel Haskel

Advanced Photon Source, Argonne National Laboratory, Argonne, IL 60439, USA

INDEX

1 INTRODUCTION

The application of synchrotron radiation to the study of magnetic materials has grown rapidly in recent years, owing in part to the availability of high-brightness synchrotron sources around the world. Several characteristics of synchrotron radiation make the study of magnetic materials very attractive. First of all, the high brightness of the beam typically results in a flux of 10^{13} photons/sec in less than a 1 mm^2 area, which enables the study of very small or highly diluted samples. The naturally high scattering wave vector resolution due to high degree of x-ray collimation and monochromaticity allows for very precise determination of magnetic modulations. Furthermore, the well-defined polarization characteristics of synchrotron radiation (linear in the plane of the particle orbit), together with its relatively simple manipulation and analysis by crystal optics, can be used to study a variety of magnetization states. Lastly, by tuning the energy of the incident beam near absorption edges (or resonances) of constituent elements, one can study the magnetic contributions of individual components in heterogeneous structures.

X-rays interact with matter through scattering from both the electron's charge and its magnetic moment. The scattering from the charge is the dominant term and is the basis for most condensed matter studies using x-rays. Although small, the scattering form the magnetic moment is sufficient to extract valuable information on magnetic structures in single crystals (Gibbs, 1985; McMorrow, 1999). Enhanced sensitivity to magnetic moments can be achieved by tuning the x-ray energy to selected resonances. These resonant enhancements have resulted in wide spread applications of x-rays in the study of magnetism, both in the absorption (x-ray magnetic circular dichroism) (Schütz, 1988; Chen, 1990) and scattering (x-ray resonant magnetic scattering) (Namikawa, 1985; Gibbs, 1988) channels. These include studies of interfacial magnetic roughness in multilayers (Freeland, 1999; Nelson, 1999; Lee, 2003a, 2003b), and morphology of magnetic domains in buried interfaces (Pollmann, 2001; Lang, 2001), just to mention a few examples. Furthermore, by performing polarization analysis of the scattered radiation (Gibbs, 1991) or applying sum rules to dichroic spectra of spin-orbit split absorption edges (Chen, 1995), one can distinguish between spin and orbital contributions to the magnetic moment in an element-specific way. This is in fact a unique attribute of magnetic scattering and

spectroscopy techniques, and it is the primary reason why these techniques are powerful tools in magnetism studies.

Most synchrotron studies of nanomagnetism have been performed using soft x-rays (loosely defined as less than 3 keV) since resonant dipolar transitions in this energy regime access electronic states carrying large magnetic moments in most materials (e.g. *3d* states in transition metals and *4f* states in rare-earth compounds). Hence, the magnetic signals are larger and easier to observe. Harder x-ray energies (>3 keV) access electronic states with smaller, yet significant, magnetic moments (e.g. 4p states in transition metals and 5d states in rare-earth compounds). While experimentally more challenging, hard x-ray studies of magnetism offer unique advantages. The higher penetrating power of these x-rays enables the study of buried structures and interfaces, which can be important in characterizing a wide variety of systems used in modern technologies, such as permanent magnetic materials and artificial thin film heterostructures. The penetrating power of hard x-rays yields a true bulk measurement probe without the need for high-vacuum conditions while soft x-ray measurements are surface sensitive and must be performed in UHV conditions. Furthermore, the short x-ray wavelengths permit diffraction studies to probe the magnetic order in both crystals and artificial, periodic nanostructures such as multilayers and patterned dot/hole arrays.

The rich polarization dependence of magnetic scattering is commonly used to extract the magnetic ordering of a material. Antiferromagnetic (AFM) structures are commonly studied with linearly polarized radiation. In the absorption channel, the linear dichroism effect (van der Laan, 1986; Stöhr, 1998) results in absorption contrast for parallel and perpendicular alignments of x-ray's linear polarization and sample's magnetization in the presence of magneto-crystalline anisotropy, which can be used, e.g., to image AFM domains in exchange-biased systems (Scholl, 2000). In the diffraction channel, AFM ordering results in Bragg diffraction at the magnetic ordering's wave vector, since the x-rays' magnetic field couples to the ordered electron spins. As discussed below, while this coupling is relatively weak, synchrotron radiation brightness, together with resonant enhancement of the magnetic scattering cross section, results in easy detection of x-ray magnetic scattering from AFM-ordered systems at third-generation synchrotron sources. Circularly polarized (CP) radiation can also be useful in studies of AFM materials. An example where CP x-rays were used for real-space imaging of chiral domains by

helicity-dependent Bragg scattering from the spiral AFM state of a holmium crystal is included in Section 2 below (Lang, 2004).

Ferri- or ferromagnetic (FM) structures are commonly studied with circularly polarized (CP) radiation. In the absorption channel, magnetic circular dichroism results in absorption contrast for parallel and anti-parallel alignment of x-ray's helicity and sample's magnetization (Schütz, 1987). By measuring this absorption contrast through spin-orbit split core levels (e.g., L_2 and L_3 edges), element-specific magnetic moments in the final state of the absorption process (both spin and orbital components) can be extracted through the application of sum rules (Thole, 1992; Carra 1993). This contrast, in combination with focused x-ray beams, can be used to image FM domains in nanostructures. Examples of such imaging studies in buried spring-magnet structures are shown in Section 4. Diffraction contrast for opposite helicities of CP radiation can also be used to study FM structures. While this differential measurement removes pure chemical scattering, without polarization analysis it results in charge-magnetic interference scattering (Blume, 1988). This interference scattering contains information on both magnitude and direction of magnetic moments. Examples wherein this interference signal is used to obtain magnetization depth profiles across buried interfaces in artificial Gd/Fe nanostructures, and site-specific magnetism in crystals, are presented in Sections 3 and 4 below (Haskel, 2001, 2004).

Our chapter is organized along the commonly used synchrotron techniques. In Section 1, the cross section for x-ray scattering is outlined and its dependence on sample's magnetization state emphasized. In Section 2, studies of site-specific magnetism and spiral antiferromagnetic domains with diffraction techniques are presented. In Section 3, the use of reflectivity techniques to probe buried interfacial magnetism is demonstrated. Finally, in Section 4, spectroscopy was used to image magnetic domains, study inhomogeneous magnetization profiles and perform vector magnetometry in patterned arrays. Although there are many more examples that illustrate the utility of hard x-ray characterization techniques in magnetism studies, our goal is to familiarize our readers with some of the tools that might benefit their own research.

1.1. X-ray scattering cross section

The general expression for the scattering of x-rays from atomic electrons in a periodic medium is given by (Blume, 1988),

$$\frac{d\sigma}{d\Omega} = r_o^2 \left| \sum_n e^{i\vec{Q}\cdot\vec{r}} f_n\left(\vec{k},\vec{k}',\hbar\omega\right) \right|^2,$$
Eq. 1.1.1

where $\vec{r}$ is the position of the atom in the crystal, $\hbar\omega$ is the incident photon energy and Q=k-k' is the scattering vector. The scattering amplitude per atom, f, consists of several contributions,

$$f\left(\vec{k},\vec{k}',\omega\right) = f^{charge}\left(\vec{Q}\right) + f'\left(\vec{k},\vec{k}',\omega\right) + if''\left(\vec{k},\vec{k}',\omega\right) + f^{spin}\left(\vec{k},\vec{k}',\omega\right).$$
Eq. 1.1.2

Here f^{charge} is the usual Thompson scattering, f' and f'' are the energy-dependent anomalous contributions and f^{spin} is the scattering from the spin of the electrons. For a typical hard x-ray energy of 10 keV, the pure spin magnetic scattering amplitude is down by 0.02 relative to Thomson scattering, i.e., four orders of magnitude reduction in the scattering cross section. The small ratio of magnetic to nonmagnetic electrons reduces the magnetic scattering even further, typically by 5-6 orders of magnitude depending on the net magnetic moment. Although small, this signal can be easily observed in systems where the magnetic modulation is different than the charge, such as in AFM structures. Further the strength of the magnetic scattering can be strongly enhanced near a resonance, as described below.

Depending on the energy of the incident x-ray radiation, two regimes can be distinguished: the nonresonant regime where the incident energy is far away from the excitation energy of absorption edges of constituent atomic species, and, the resonant regime, where the incident energy is close to an absorption edge. Although all examples given in this chapter belong to the latter, a formalism describing the nonresonant regime will be introduced first, followed by its extension into the resonant limit.

1.1.1. Nonresonant cross section

Far from a resonance, the magnetic dependence of the anomalous contributions can be separated, reducing the expression for the scattering amplitude into two terms, one containing the interaction with the charge of the atom and another containing its interaction with the magnetic

moment. These two terms derived from second-order perturbation theory (Blume, 1985, 1988, 1994) are given below,

$$f = f^{ch\arg e} + f^{magnetic} = \rho(Q) \; \hat{\varepsilon}' \cdot \hat{\varepsilon} + ir_o \left(\frac{\hbar \omega}{m_e c^2} \right) \left[\frac{1}{2} \vec{L}(Q) \cdot \vec{A} + \vec{S}(Q) \cdot \vec{B} \right].$$
Eq. 1.1.1.1

Here $\rho(Q)$, $S(Q)$, and $L(Q)$ are the Fourier transforms of the electrons charge, and the spin and orbital magnetic moments, respectively. *A* and *B* are matrices (see Blume and Gibbs, 1988) that contain the polarization dependence of the magnetic scattering, which differs from that of the charge scattering. In principle, this polarization dependence can be exploited to obtain quantitative information on the size of the magnetic moments responsible for the scattering. In practice, however, this information is typically limited to AFM structures, where the magnetic scattering is separated from the charge scattering in reciprocal space. Therefore, most studies of FM materials are performed using resonant scattering and absorption as described below.

1.1.2. Resonant cross section

When the energy of the incident photon is near an absorption edge, additional resonant terms contribute to the x-ray scattering (Gibbs, 1988; Namikawa, 1985; Hannon, 1988). These resonances occur at energies sufficient to promote deep-core electrons into states at and above the Fermi level (Figure 1.1). This results in a large increase in the x-ray scattering cross section for a material due to an energy difference denominator in this second order process, resulting in increased absorption and an enhancement of the magnetic scattering. In other words, the enhancement in the magnetic x-ray scattering results from virtual transitions to excited, intermediate, resonant states near the Fermi level. In magnetic materials these states are spin polarized leading to an increase in the sensitivity of the scattering to the magnetism of the scattering atom. This additional scattering results in the anomalous term in eq. 1.1.2. The resonant scattering amplitude can be calculated using the following expression (Hannon, 1988),

$$f_{EL} = 4\pi\lambda \sum_{M=-L}^{L} \left[\varepsilon_f^* \cdot Y_{LM} Y_{LM}^* \cdot \varepsilon_i\right] F_{LM}.$$
<div align="right">Eq. 1.1.2.1</div>

Here ε is the beam polarization, Y_{LM}'s are vector spherical harmonics, and F_{LM} are the matrix elements involved in the transition. In general, different multipole order transitions can contribute to the resonant enhancement. In most cases, however, the electric dipole transitions dominate, yielding the following simple expression for the scattering amplitude (Hannon, 1988; Hill, 1996),

$$f^{res} = F^0\left(\hat{\varepsilon}_f \cdot \hat{\varepsilon}_i\right) - iF^1\left(\hat{\varepsilon}_f \times \hat{\varepsilon}_i\right) \bullet \hat{m}_n + F^2\left(\hat{\varepsilon}_f \cdot \hat{m}_n\right)\left(\hat{\varepsilon}_i \cdot \hat{m}_n\right).$$
<div align="right">Eq. 1.1.2.2</div>

Here the F^n are complex quantities containing the amplitude of the scattering given by the matrix elements of the transitions involved, ε are the initial and final polarization vectors and $\hat{m}$ is the direction of the magnetic moment of the atom. The first term above is the charge anomalous
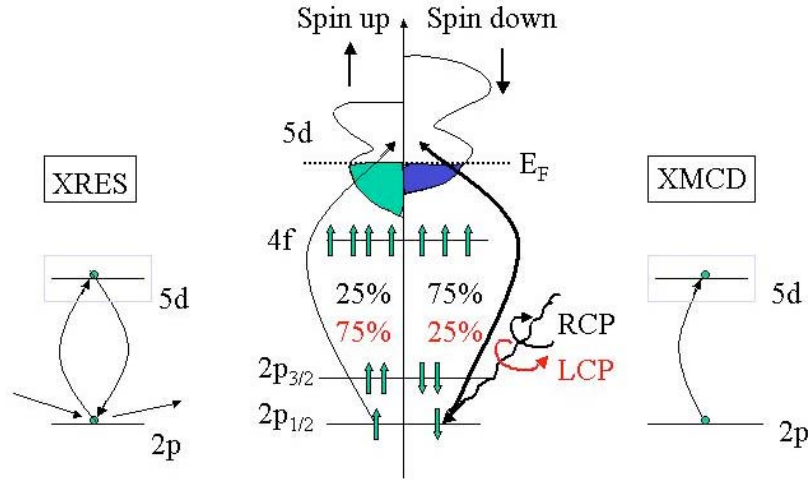

Figure 1.1 Illustration of the resonant scattering (left) and absorption (right) of x-rays. Absorption involves the photoexcitation of an electron to an energy above the Fermi level, while resonant scattering involves a virtual transition through a similar intermediate state. For circularly polarized incident x-rays the transition probability to spin-up(-down) states is different leading to magnetic sensitivity.

scattering amplitude, whose polarization dependence is the same as that for Thompson scattering. The second term is linear in the magnetization and therefore can be isolated by reversing the magnetization of the sample and measuring the difference in the absorption or scattering. Similarly this term leads to differences in the scattering and absorption for circularly polarized x-rays, and its imaginary component is responsible for circular magnetic x-ray dichroism (XMCD) in absorption measurements. The last term is quadratic in the magnetization and is typically much smaller than the F^1 term. This term is responsible for linear dichroism effects.

2. DIFFRACTION TECHNIQUES

The intrinsic periodicity d of atomic arrangements in crystals, interfaces in layered structures, and lithographically patterned arrays of periodic nanostructures (dots, antidots, rings) results in diffracted intensity at Bragg conditions associated with that periodicity ($2d\sin\theta=\lambda$). While the atomic-scale periodicity of crystals ($d\approx 1\text{Å}$) results in Bragg reflections at relatively large angles, the much larger periodicity of artificial multilayers or lithographically patterned arrays of magnetic elements ($d\approx$5nm-1μm) results in small-angle diffraction. Nonetheless, since x-rays scatter from atomic electrons in crystals and from interfaces in layered structures, this diffracted intensity contains information about the electronic atomic charge density in crystals or electronic density contrast at the interfaces of artificial layered structures. As pointed out in the introduction, while the x-ray's magnetic field does not couple strongly to the magnetic moment of electrons, large resonant enhancements of magnetic-sensitive scattering of x-rays can be achieved near the absorption threshold for resonant transitions between a deep-core electron level and electronic orbitals near the Fermi level, which carry magnetic moments. This magnetic resonant scattering is much stronger, 10^{-1}-10^{-3} of the charge scattering (for hard x-rays), and contains information on the resonating element's magnetic moment. In the following examples, we exploit the periodicity of the magnetic structure under study and the enhanced sensitivity of resonant magnetic scattering to first zoom into the atomic origins of magnetocrystalline anisotropy in single crystals of $Nd_2Fe_{14}B$ permanent magnet, and, second, to image chiral antiferromagnetic domains in holmium single crystals.

2.1. Site-specific magnetism in ferro (ferri)-magnetic crystals

The ability of x-ray spectroscopic techniques to separate the magnetic contributions from different elements in heterogeneous systems; i.e., element specificity, has proven remarkably useful in disentangling the complex magnetic behavior encountered in systems of current fundamental and technological interest.

The complexity of magnetic materials, however, goes beyond the presence of multiple elements: this includes materials where elements of the same specie reside in inequivalent crystal sites (such as magnetite Fe_3O_4, with octahedral and tetrahedral Fe sites), and nanocomposite materials, where elements of the same specie occur in more than one nanocrystalline phase (such as $Nd_2Fe_{14}B/\alpha$-Fe exchanged coupled nanocomposites). Current developments are aimed at extending the ability of x-ray-based techniques past element specificity towards site- and phase-specific magnetism. In particular, we show how basic crystallography can be combined with resonant scattering of CP x-rays to extract element- and site-specific magnetism in crystals.

In magnetic materials, the resonant (anomalous) scattering of CP x-rays is modified from that in nonmagnetic materials. This is because the virtual photoelectron that is excited from the core state to the intermediate, resonant, state is partially spin polarized and therefore becomes sensitive to the spin imbalance in the density of states at the intermediate state near the Fermi level. The inherent element specificity of this resonant scattering can then be combined with structure factor effects in crystals to enhance/suppress scattering from selected lattice sites. Here we exploit the symmetry properties of a crystal of $Nd_2Fe_{14}B$ to study the magnetization reversal of the two inequivalent Nd sites in this structure (*4f* and *4g* sites in Wyckoff notation). The permanent magnet of choice for many applications is $Nd_2Fe_{14}B$. Its magnetic hardness, i.e., its resistance to demagnetizing fields, has its origins at the atomic level and is due to the large orbital moment at Nd sites (predominantly from 4f atomic shells) interacting with the crystal field of the lattice. Since inequivalent Nd sites reside in quite distinct atomic environments, they experienced different crystal fields (Herbst, 1991) and therefore are expected to display different local magnetocrystalline anisotropy. There is currently no technique that can directly measure the magnetic response of these distinct sites separately.

Wyckoff Site	(110)	(220)	(440)
4f	2.2+0.5i	140+35i	86+29i
4g	69+15i	5.2+1.3i	92+31i

Table 2.1.1. Calculated site-specific Nd structure factor for selected Bragg reflections. Resonance charge contributions to the structure factor at the Nd L_2 resonance are from tabulated values. Structural parameters are from (Herbst, 1991).

Site selectivity is achieved by exploiting the symmetry properties of the crystal. $Nd_2Fe_{14}B$; has a $P4_2/mnm$ tetragonal space group with four formula units per unit cell. The 56 Fe atoms are distributed among six inequivalent sites while the 8 Nd atoms occupy two other inequivalent sites (*4f, 4g*). As shown in Table 2.1.1, by selecting scattering vectors along the high-symmetry [110] direction, structure factor contributions from either one or the other Nd sites nearly vanish. Diffraction from (110) planes probes Nd at *4g* sites since scattering from the four *4f* sites interferes destructively. The opposite is true for a (220) diffraction condition, while nearly equal contributions of the two Nd sites are measured at a (440) Bragg reflection.
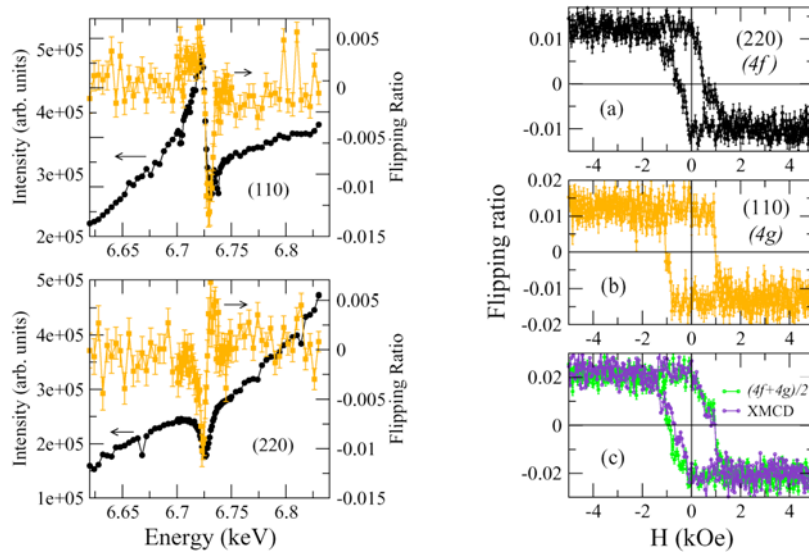

Fig 2.1.1 (Left) Resonant diffraction through the Nd L_2 absorption edge for (110) and (220) diffraction conditions. Black data are charge (chemical) scattering; yellow data are magnetic sensitive scattering. At each Bragg condition, only one inequivalent Nd site is visible; the scattering contributions from the other add destructively. (Right) Top two panels show element- and site-specific Nd hysteresis loops obtained on each reflection. Bottom panel shows the average of two reflections and the loop obtained from the XMCD signal.

The $Nd_2Fe_{14}B$ single crystal was placed in the 6 kOe applied field of an electromagnet, and measurements were carried out at room temperature. The crystal was aligned with its [110] direction along the scattering vector and the magnetic field applied along the [001] easy-axis direction, which was parallel to the sample surface and in the scattering plane. Resonant diffraction was measured through the Nd L_2 edge by switching the helicity of the incident CP x-

rays at every energy point while maintaining a given diffraction condition (fix Q) at all energies. XMCD measurements were simultaneously performed by measuring the difference in Nd L_β fluorescence for opposite helicities using Ge solid-state detectors. Element- and site-specific hysteresis loops were performed at the different diffraction conditions by recording changes in scattering intensity as a function of applied field for opposite helicities of CP x-rays.

Figure 2.1.1 shows resonant diffraction data taken under (110) and (220) Bragg conditions. These reflections alternately probe *4g* and *4f* sites, respectively. The resonant charge scattering is obtained from $(I^+ + I^-)$, while the charge-magnetic interference scattering (Haskel, 2004) is obtained from the flipping ratio $(I^+ - I^-)/(I^+ + I^-)$. This interference scattering is proportional to the magnitude of the magnetic moment and also contains information about the moment's direction relative to the x-ray polarization vectors . Here (I^+, I^-) are scattered intensities for opposite x-ray helicities.

Modeling of the charge-magnetic interference scattering should allow separation of chemical and magnetic anomalous scattering factors for each of the Nd sites. This will yield unique quantitative information on the size of the magnetic moment and on the chemical valence state at each site. Spectroscopic information, such as differences in the spin polarization of unoccupied Nd *5d* states at both sites, is included in the imaginary parts of the magnetic anomalous scattering factors. Current work is focused on developing the required algorithms needed to retrieve this information. While deriving magnetic information from the energy-dependent scattering requires accurate modeling of the interference of charge and magnetic scattering, field-dependent measurements relax this constraint and allow for studies of the magnetic response at each site to be recorded by working under either one diffraction condition for selected energies that maximize the magnetic contrast at each site. This is also shown in Figure 2.1.1, where site-specific hysteresis loops are shown. They show that the magnetic moment at Nd *4g* sites requires a significantly larger reversed applied field and reverses more sharply than those at Nd *4f* sites. This clearly shows the Nd *4g* sites are predominantly responsible for the magnetocrystalline anisotropy (MCA) providing unprecedented detail into the atomic origins of MCA in $Nd_2Fe_{14}B$. The same figure also compares the weighted average of the magnetic signals at each site with the XMCD measurement. Since the absorption-based XMCD signal intrinsically averages over the two sites, the good agreement provides self-consistency. In addition, we measured the same reversal curves in both diffraction and

absorption channel for (440) Bragg reflections as expected due to the equal scattering contributions of Nd sites at these Q vector (Table 2.1.1). The different magnetic responses of Nd sites are likely due to the different crystal fields arising from the unequal crystalline environments. For the two reflections shown here, the polarization dependence of the charge-magnetic interference signal yields a near-zero signal when the magnetization is along [110] direction. This implies that at a reversed applied field of 500 Oe the magnetizations of Nd *4g* and *4f* sites are nearly orthogonal to one another (the *4g* site is still magnetized along the [001] direction at this field). The ferromagnetic Nd-Nd coupling in this material is indirect and weak, through exchange interactions with the surrounding Fe ions and the spin polarization of conduction electrons. The magnetization reversal process, which is dominated by competing MCA at the two Nd sites and the Nd-Fe exchange, is nontrivial, as seen in Fig. 2.1.1. The MCA strongly affects the reversal process, which includes largely static noncollinear configurations of Nd moments. It is likely that Fe moments mediating the Nd-Nd coupling participate in this unconventional reversal mechanism as well.

In summary, this example demonstrates the potential of combining the spectroscopic signatures inherent in resonance x-ray scattering with structure factor effects in crystals to obtain element- and site-specific magnetism in crystals. This method allows obtaining information on the atomic origins of MCA and can be applied to both crystals and epitaxially grown films. Extension of this method to phase-specific magnetism in nanocomposite magnetic structures with multiple crystalline phases is currently under way.

2.2. Imaging spiral magnetic domains

Many techniques have been developed to image magnetic domains (Celotta, 2001), but most measure either ferromagnetic or linear antiferromagnetic structures. A wide variety of materials, however, exhibit more exotic magnetic ordering, particularly materials that contain rare-earth elements. These exotic magnetic structures can exhibit their own unique domain structures within a material. Hard x-rays can be used to image such domains through the use of microfocusing optics in conjunction with resonant magnetic x-ray scattering techniques.

Spiral antiferromagnets form one particular type of such structures, where the moments align in ferromagnetic planes within an atomic layer but rotate by a characteristic angle between successive layers along the magnetic propagation direction. The sense of this rotation can be either right or left handed leading to the formation of chirality domains within the sample. Holmium metal offers one example of such a magnetic structure. Holmium orders in the spiral structure below T_N=133K, with the propagation direction along the

T < 19°K   19 < T < 133°K

Figure 2.2.1   The low-temperature conical (left) and high-temperature basal plane spiral (right) magnetic structure of Ho.

c-axis of the hexagonal unit cell. Below T=19K, the moments cant away from the basal plane forming a conical structure (figure 2.2.1). This magnetic superstructure results in the appearance of satellite peaks on either side of the charge Bragg diffraction peaks at $(0,0,L\pm\tau)$. At these

magnetic peaks, circularly polarized x-rays become sensitive to the handedness of such a helix (i.e., either right or left handed) (Blume 1988; Sutter, 1997). Therefore, contrast between magnetic domains of opposing handedness can be obtained by reversing the incident beam helicity and measuring the difference in the Bragg scattering intensity.

A measure of this sensitivity to spiral helicity is shown in figure 2.2.2, which shows the energy dependence of the intensity and helicity contrast at the (0,0,4+t) peak near the Ho L_3 absorption edge resonance. Near this resonance, the intensity of the magnetic scattering is strongly enhanced (top of figure 2.2.2) and the sensitivity of helicity reversal to spiral handedness varies dramatically. The
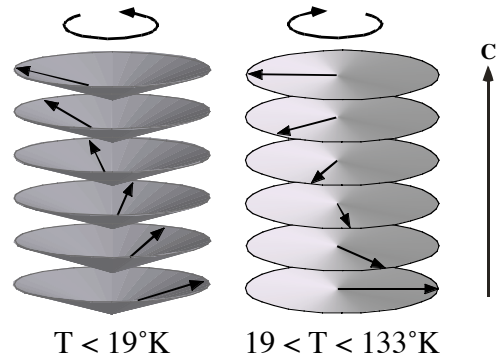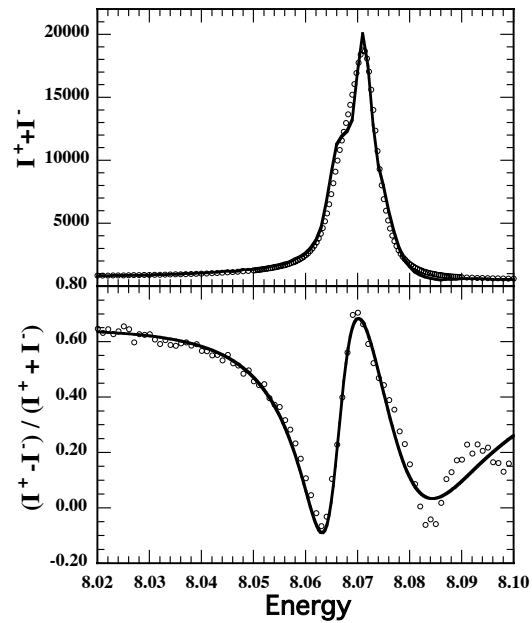

Figure 2.2.2   Scattering intensity of the magnetic peak with a circularly polarized incident beam. Top: Total counts. Bottom: Normalized difference. Lines: Theory.

14

maximum contrast of about 75% occurs about 1eV below the peak of the scattering intensity, with contrast strongly suppressed on either side of the resonance. Away from the resonance, the contrast was similar to that at the peak, but, while it quickly approached this value below the edge, the contrast suppression persisted for over a hundred eV above the edge.

A 640μmx500μm image of the chiral domain structure of Ho obtained at the $(0,0,4+\tau)$ magnetic peak is shown in figure 2.2.3. This image was obtained using slits to define a $25x25μm^2$ immediately before the sample. The Ho crystal was placed inside closed-cycle He refrigerator, mounted to a Huber psi-circle goniometer. The sample was oriented on a magnetic Bragg peak and then the sample was scanned through the beam, reversing the helicity at each point to obtain an image of the helicity domains. The domain features exhibit a characteristic length scale on the order of 100 μm and are uncorrelated with the crystal lattice (a axis was oriented up in the figure). Warming the sample past T_N and recooling nucleated a completely different domain pattern indicating that crystalline defects play very little role in the nucleation of spiral domains.
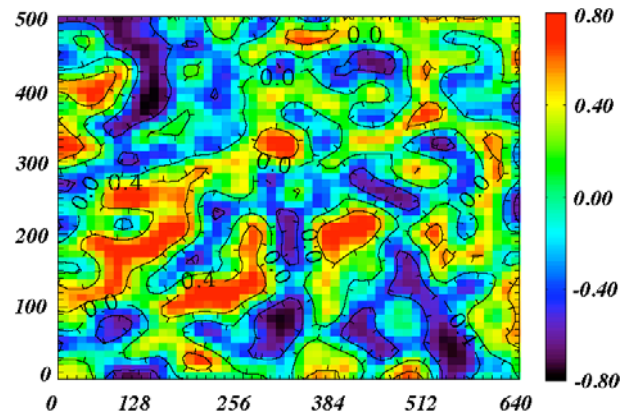

Figure 2.2.3 $640x500μm^2$ spiral domain pattern in Ho metal at 10 K.

15

3. REFLECTIVITY TECHNIQUES

In this section, the study of inhomogeneous magnetic profiles in Fe/Gd multilayers with polarized hard x-rays is presented. Experimental results are supported by theoretical work on modeling interfacial magnetism. The question of magnetic roughness and its correlation with chemical roughness will be discussed, since it is one of the important questions in the design of new-generation electronics devices which utilize the spin of electrons (Awschalom, 2002).

3.1   Studies of interfacial magnetism with circularly polarized x-rays

Understanding chemical and magnetic properties of buried interfaces in layered systems is of great scientific and technological interest. For example, chemical interfacial roughness affects spin-polarized transport and related giant magnetoresistance effects in spin valves (Schad, 1998). Interfacial magnetic disorder accompanying chemical disorder introduces uncompensated spins at ferromagnetic-antiferromagnetic exchange-biased interfaces affecting magnetization reversal processes (Bae, 2000). Our goal in this example is to show how one can *quantify* fundamental properties of buried magnetic interfaces, including strength and extent of interlayer exchange coupling and chemical and magnetic roughness.

X-ray specular reflectivity has been widely used to extract charge density profiles in layered structures. Since, in the x-ray regime, a material's index of refraction is always slightly less than one, total external reflection below a critical angle is the norm contrary to the total internal reflection commonly found at interfaces between media in the optical regime. The reflected intensity is almost unity below the critical angle for total external reflection but decreases sharply with increased scattering angle as Q^{-4} (Q is scattering vector $Q=4\pi/\lambda \sin\theta$). In the hard x-ray regime, this results in significant reflected intensity only at small scattering angles $\theta \leq 10°$. Since the associated scattering wave vectors are much smaller than the inverse of typical interatomic distances, the atomic structure can be neglected and scattering occurs at the interfaces between media with different indices of refraction (charge density). The specular reflectivity is related to the Fourier transform of the charge density profile along the scattering

vector, i.e., the normal to the sample surface. X-ray resonance magnetic reflectivity (XRMR), which is a special case of x-ray resonance exchange scattering (XRES), measures the difference in specular reflectivity between left- and right-CP x-rays. Much like x-ray reflectivity yields charge density profiles in layered structures, XRMR is related to the Fourier transform of the magnetization density profile along the normal direction. Modeling of both signals allows for chemical and magnetic density profiles to be retrieved, including the position of chemical and magnetic interfaces and their chemical and magnetic roughness. In contrast, the absorption-based XMCD measures the difference in absorption coefficient between opposite helicities of x-rays and averages over the magnetization depth profile provided the x-ray penetration depth at
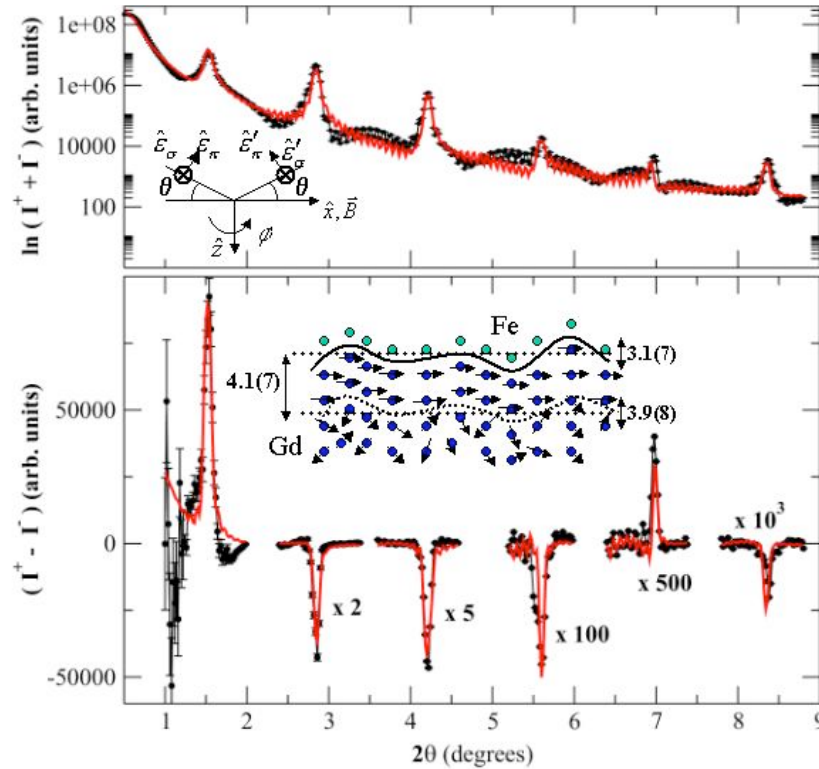

Figure 3.1.1. Charge (top) and charge-magnetic interference (bottom) specular reflectivity (points) and fits (lines) for E=7929 eV and 300K across six multilayer Bragg peaks. Top inset shows scattering geometry and applied field direction. Bottom inset shows the derived interfacial magnetic structure. The Gd/Fe interface has both charge and magnetic roughness (same within uncertainties); ferro-paramagnetic interface has only magnetic roughness (all units Å). This experiment probes the Gd magnetization only.

the measurement incident angle is larger than the sample thickness, which is usually the case for magnetic thin films and incident angles larger than a few degrees.

We illustrate the application of this techniques on a [Fe(15Å)Gd(50Å)]$_{15}$ multilayer sample that was sputtered in vacuum onto a Si substrate using Nb buffer (100Å) and cap (30Å) layers. Since Gd and Fe have similar bulk magnetizations, 2020 and 1750 emu/cm^3, respectively, the much thicker Gd dominates the magnetization at low temperatures, and its magnetization aligns with an applied field. A strong antiferromagnetic interlayer exchange coupling forces the Fe into an anti-parallel alignment. SQUID magnetometry shows that Gd dominates the magnetization up to at least 350K, i.e, well above its bulk Curie temperature of 293K. The markedly different Curie temperatures of Gd and Fe (1024K) allow us to distinguish Gd "bulk" and interfacial regions by tuning the sample temperature. More generally, it allows the investigation of proximity effects between low- and high-T_c ferromagnets at the atomic scale.

Figure 3.1.1 shows specular reflectivity curves measured near the Gd L$_2$ edge at T=300K, as obtained by adding (top) and subtracting (bottom) scattered intensities for opposite helicities of the incoming CP radiation. The sum yields the charge reflectivity curve related to interference between x-rays scattered from variations in the charge density depth profile; the difference is due to interference between x-rays scattered from both charge and magnetic density variations, as explained below.

The difference signal was modeled within the first Born approximation (BA), which assumes weak scattering and is valid away from the regime of total external reflection. Combining equation 1.1.2.1 from Section 1 with the nonresonant charge scattering term from equation 1.1.1.1, the coherent resonant elastic scattering length for a single magnetic ion in the electric dipole approximation is given as a sum of a charge and a magnetic term.

$$f = (f_0 + f_e)(\hat{\varepsilon}'^* \bullet \hat{\varepsilon}) + if_m(\hat{\varepsilon}'^* \times \hat{\varepsilon}) \bullet \hat{m}. \qquad \text{Eq. 3.1.1}$$

Here f_o, f_e and f_m have substituted for $\rho(Q)$, F^0, and F^1, in the former equations. The much weaker nonresonant magnetic scattering, as well as the linear dichroism term F^2, have been neglected (the latter does not contribute to this scattering geometry). In the first BA, the difference cross section for opposite helicities of CP x-rays for a system of N interfaces with charge and magnetic roughness is given by (Sinha, 1988; Osgood, 1999):

$$\Delta_{(L,R)}\frac{d\sigma}{d\Omega} = \frac{4\pi^2 L_x L_y \delta(q_x)\delta(q_y)}{q_z^2}[\cos 2\theta(\hat{k}_i \bullet \hat{m}) + (\hat{k}_f \bullet \hat{m})] \times$$

$$\sum_{i,j}^{N} e^{iq_z(z_i - z_j)}[\Delta\rho^*_{e,i}\Delta\rho_{m,j}e^{-\frac{q_z^2}{2}(\sigma^2_{3,i}+\sigma^2_{m,j})} + \Delta\rho_{e,j}\Delta\rho^*_{m,i}e^{-\frac{q_z^2}{2}(\sigma^2_{e,j}+\sigma^2_{m,i})}]$$

Eq. 3.1.2

Where $\Delta\rho^*_{e,i} = [n_e^{i+1}(f_0+f_e^*)^{i+1} - n_e^i(f_0+f_e^*)^i]$ and $\Delta\rho^*_{m,j} = n_e^{j+1}(f_m)^{j+1} - n_e^j(f_m)^j$ are charge and magnetic density contrast at interfaces i and j, respectively. Here $f_0 = -Zr_0$ and f_e, f_m are complex, anomalous charge and magnetic scattering lengths; n_e is atomic number density and $\sigma^2_{e,m} = \langle[\delta z_{e,m}(x,y)]^2\rangle$ is the mean squared height fluctuations, assumed Gaussian, about the average position of charge and magnetic interfaces. For simplicity, the cross section above neglects phase retardation and absorption effects; these are included in the fits (Haskel, 2001). For magnetically aligned phases (collinear) the polarization factor involving the local magnetization *direction* is constant throughout the Gd layer thickness at fixed q_z. The *magnitude* of the local magnetization is allowed to vary through the resonant f_m.
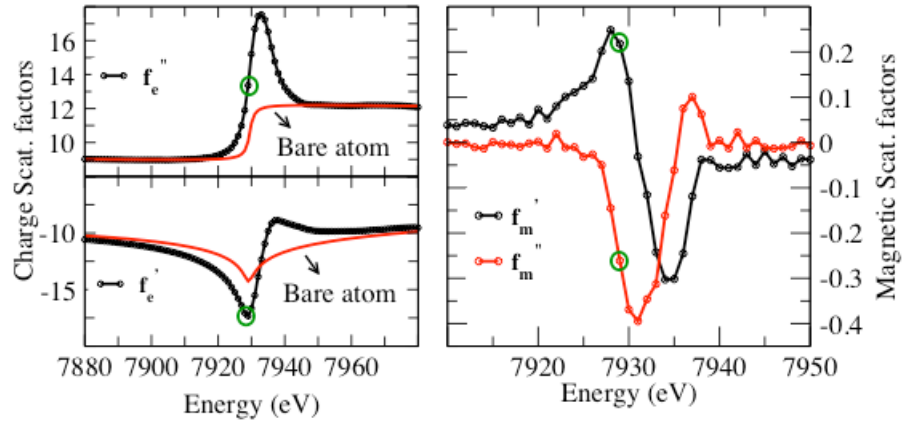

Figure 3.1.2. Determination of resonant charge and magnetic scattering factors near the Gd L_2 edge. Edge-step normalized charge (μ_e) and magnetic (μ_m) absorption coefficients (left panel) are combined with tabulated bare-atom scattering factors away from resonance to derive $f''_{e,m}(E)$ and KK-related $f'_{e,m}(E)$ (right panel). Values at the resonant energy (7929 eV) used in the magnetic reflectivity measurements shown with circles.

Quantitative analysis requires accurate values of complex charge and magnetic anomalous scattering factors at the resonant energy. Their strong energy dependence, which includes solid state (band structure) and excitonic (core-hole) effects calls for their experimental determination on the actual structure under study. Through the optical theorem, the imaginary parts of these factors are related to the absorption coefficient by $f''_{e,m}(E) \propto (e/r_0 n_e hc)\mu_{e,m}(E)$. We measured the energy dependence of the absorption coefficient at 16K in a 100 eV interval around the Gd L_2 edge for opposite helicities of CP x-rays, $\mu^{\pm}(E)$, to obtain edge-step normalized $f''_{e,m}$ ($\mu_e=[\mu^++\mu^-]/2$, $\mu_m=\mu^+-\mu^-$) and used bare-atom scattering factors *away* from resonance for absolute normalization. Real parts were obtained from differential Kramers-Kronig (KK) transforms of imaginary parts.
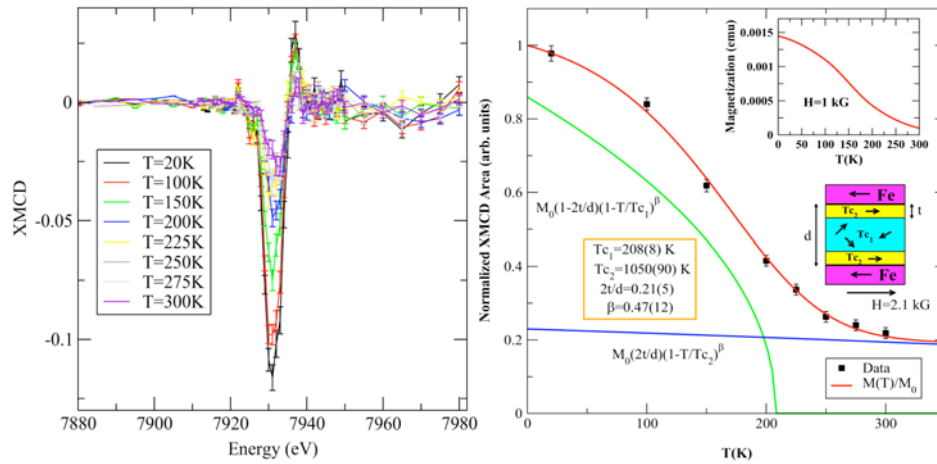

Figure 3.1.3. XMCD signal (left) and integrated XMCD area (points, right) at the Gd L_2 edge. Integrated intensities are fitted as a superposition of interfacial and bulk regions with same saturation magnetization M_0 but variable T_c and volume fractions. Fit (red line) includes a convolution with a Gaussian to account for disorder in the sputtered layers. Top inset shows SQUID magnetization data.

Magnetization density profiles in the Gd layers are described (through variations in f_m) in terms of a few fitting parameters, which are then refined in a nonlinear least-squares fitting of the BA cross section to the data. The most significant finding is summarized in the inset of figure 3.1.3 At 300K, best fits indicate that Gd is paramagnetic except for a region 4.1(7)Å in size that remains fully magnetized near the Gd/Fe interface. This magnetization is induced by a strong anti-ferromagnetic interaction with the magnetically ordered Fe layer, as predicted in mean-field

calculations by Camley (1989). This size is a measure of the spatial extent of the AFM interaction at the Gd/Fe interface.

The presence and size of this ordered Gd region were confirmed by T-dependent XMCD measurements. Figure 3.1.3 shows the XMCD signal at the Gd L_2 edge (left panel) together with its integrated intensity (points, right panel). At 300K, the Gd layers retain $\approx$ 20% of their saturation magnetization, consistent with the magnetic reflectivity result of $\approx$ 17% of the layer volume remaining magnetized at 300K. By modeling the XMCD as a superposition of interfacial and "bulk" regions with variable volume fractions and T_c values, we find a 5.2±1.2Å region remains magnetized at 300K with an estimated T_c=1050(90)K. Since this magnetized region is induced by the strong AFM exchange interaction at the Gd/Fe interface, its T_c value quantifies the strength of this interaction; i.e., $J_{AF} \approx J_{Fe} \approx$ 1000K. An enhanced T_c of $\approx$ 800K was previously reported for one monolayer of Gd on a Fe(100) substrate (Taborelli, 1986).

In summary, this example demonstrates the ability to quantify with high accuracy fundamental parameters characterizing a buried magnetic interface in a layered system. This includes the spatial extent and strength of interfacial exchange coupling and interfacial magnetic roughness. Future effort could be directed towards gaining a better understanding of the interfacial electronic and atomic structure. Spin-dependent x-ray absorption fine structure (Schutz, 1989) and XMCD combined with the x-ray standing wave technique (Kim and Kortright, 2001) should provide further insight into this question.

4. SPECTROSCOPY TECHNIQUES

While x-ray resonant scattering contains spectroscopic information through its dependence on the spin polarization of the empty density of states (DOS) at the Fermi level, the retrieval of this information is not always simple. This is particularly true in cases where charge-magnetic interference scattering is measured, and, therefore chemical and magnetic spectroscopic signatures are mixed and need to be deconvolved in order to extract purely magnetic information. Magnetic spectroscopy in the absorption channel, through the x-ray magnetic circular dichroism effect, is, on the other hand, a pure magnetic signal that directly relates to the asymmetry in the DOS at the Fermi level between spin-up and spin-down empty electronic states with a particular orbital character dictated by dipole selection rules that connect the core electron state with the final state. The size of the measured XMCD signal is proportional to the degree of circular polarization in the incident beam, the magnetization of the sample, and the projection of the moment onto the incident photon direction. As such, it can be used to measure the magnetization of a sample as a function of temperature or field. In this manner, XMCD measurements are similar to those taken with a magnetometer. There are two key differences, however, between XMCD and magnetometry. First, XMCD is element specific; therefore the changes in the XMCD signal strength are proportional to the changes in the magnetization of only the particular atomic species excited at the absorption edge where the measurements are taken. Second, the angle between the applied magnetic field and the incident photon direction can be varied. This is useful in measuring magnetic structures in which the magnetic moments are not collinear with the applied field direction. Furthermore, by using a highly focused beam, the XMCD signal can be used to probe the local magnetization of the sample.

In this section, we present a series of examples where the XMCD effect was used to retrieve just such element-specific magnetic information on nanostructured materials. These include magnetic domain mapping in a Fe/SmCo exchange spring magnet, measurement of spin configuration in a Fe patterned array and determination of an inhomogeneous magnetic state in Fe/Gd multilayers.

4.1. Magnetic domain mapping of buried nanostructures

Composites of soft and hard magnetic materials have shown a great deal of promise as new high-strength permanent magnets. In these composites, the soft magnet provides a high magnetic saturation, whereas the magnetically hard material provides a high coercive field. Bilayers can be used as model systems to investigate the magnetization-reversal process in these composites (Fullerton, 1998), where the hard magnetic material is grown epitaxially on a substrate to provide a well-defined magnetization axis, and the soft material is overlaid on top of it. Studies of the spatial magnetic structure in such bilayers, however, have been limited to measurements of the domains in the top soft layer (Vlasko-Vlasov, 2001). This is because, the magnetic structure of the buried hard layer is inaccessible to established methods like magnetic force microscopy or magneto-optical Kerr-effect, since these techniques are highly surface sensitive. Thus the structure of the buried layer upon magnetization reversal could not be studied directly using these methods. In this experiment, a polarized x-ray microbeam (Pollmann, 2001) was used to overcome the limitations of the more conventional techniques. By using ~5 to 12 keV x-rays, the top layers of the structure are penetrated in a nondestructive manner, and the measurement of magnetic domain structure of the buried layer is achieved while an external field is applied.

The experimental setup for this experiment consisted of two parts. First, phase-retarding optics converts the linearly polarized beam from the planar undulator (a device commonly used in third generation synchrotron facilities to produce high-brightness radiation, Dejus, 2002; Chavanne, 2003) into a circularly polarized one, and second,

Figure 4.1.1 Images of the domain structure in Fe/SmCo with the corresponding positions on the magnetization curve.

focusing optics produces a micron-sized beam. A Kirkpatrick-Baez (KB) mirror pair yielded a focal spot of 9 x 22 μm^2, with ~10^{10} photons/s . One mirror focuses the beam in the horizontal direction, while the second one does it in the vertical direction. It should be noted that with a state-of-the-art microfocusing optics (Bilderback, 1994; Yun, 1999; Pfeiffer, 2002, Takano,
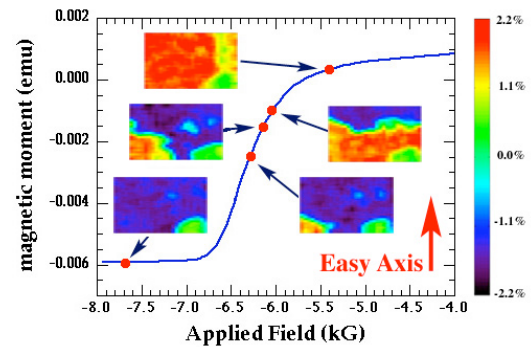
2003) and dedicated experimental setup, one can achieve a spot size of the order of 100 nm (or less) in this energy range.

X-ray magnetic circular dichroism (XMCD) was used to provide a contrast mechanism sensitive to the orientation of the magnetization. As previously described in Section 4, XMCD measures the projection of the magnetic moment onto the incident photon wave vector. Therefore, the orientation of the local magnetic moments can be measured by taking the flipping ratio $\{(I^+-I^-)/(I^++I^-)\}$ of the measured intensities for opposite helicities (this ratio is also referred to as the asymmetry ratio).

The sample studied was a 200 Å Fe/1600 Å SmCo/200 Å Fe/200 Å Ag layer grown on a MgO substrate. The SmCo was nominally deposited in the Sm_2Co_7 phase, although there are local deviations from the ideal stoichiometry, leading to $SmCo_5$ or $SmCo_3$ phases. Since the sample was grown on a relatively thick substrate, the fluorescence yield from the sample was used to measure the absorption. The fluorescence from the sample is proportional to the x-ray absorption and therefore shows XMCD contrast. Measurements

Figure 4.1.2 Hysteresis measurements for the low contrast region (red) and rest of sample (blue).

were performed at the Sm L_3 edge, monitoring the L_α fluorescence intensity. First, XMCD spectra were taken as a function of energy with an unfocused beam and the sample fully aligned. The best magnetic contrast was found to be at 6.710 keV, which was the energy then used to obtain all the magnetic structure images. Magnetic domain images were recorded as a function of the externally applied magnetic field. The sample was scanned in two dimensions through the microfocused beam. A magnetic field of up to 8 kG was applied parallel to the axis of easy magnetization.

Figure 4.1.1 shows a series of 250x500 μm^2 (vertical x horizontal) images (Lang, 2001) for different applied magnetic fields. The relative position of each image along the sample magnetization curve is also indicated. The colors in the images correspond to the measured flipping ratios given by the scale on the right. A red color denotes a region where the local magnetization is antiparallel to the incoming beam and a blue color is where it is parallel.
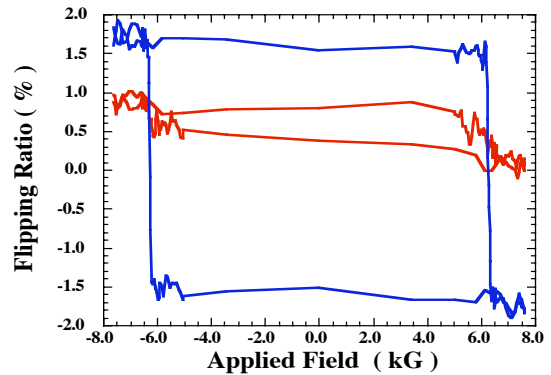
24

The images in figure 4.1.1 clearly show the magnetic reversal of the domains in the SmCo layer upon increase of the applied field. A large region (> 500 μm) nucleates at the top of the image and grows at the expense of the oppositely oriented domain. The boundary between the two domains is predominantly oriented perpendicular to the direction of magnetization. The direction of the domain wall can be understood from the chemical structure of the SmCo layer. The axis of easy magnetization in SmCo films is given by the c-axis of the Sm_2Co_7 unit cell (Fullerton, 1997). Stacking disorders induced by the $SmCo_5$ or $SmCo_3$ phases mentioned earlier will be oriented perpendicular to the easy axis. These stacking disorders may effectively pin the domain walls.

One interesting feature is found at the lower right portion of each image. In this region, very little magnetic contrast was observed for any applied fields. To investigate this further, local hysteresis measurements were performed (shown in figure 4.1.2) at the center of this region and at a point where clear domain formation was observed. Figure 4.1.2 shows that, although the contrast is much smaller than that from the other parts of the sample, there is some change in this region also. The much smaller signal is due to either a local Co deficiency in this region or a misorientation of the epitaxial growth, resulting in a crystal grain whose easy axis is oriented nearly perpendicular to the x-ray beam.

4.2. Biquadratic coupling in SmCo/Fe

Physical properties of thin magnetic nanostructures are dominated by exchange interactions between the layers. These interactions in most cases induce collinear coupling of spins. Non-collinear coupling of spins is also allowed through the biquadratic term in the exchange Hamiltonian $H_2 = -j(M_1 * M_2)^2$, where M_1 and M_2 are magnetic moments in the layers. However, the biquadratic exchange is typically much smaller than the conventional Heisenberg exchange. Recently Vlasko-Vlasov (2001), observed unusual perpendicular coupling of two ferromagnetic layers in direct contact in a now familiar system of SmCo and Fe exchange spring magnets. They deduced noncollinear remanent magnetic configurations based on magneto-optical imaging of the top Fe layer.

In this example, we demonstrate how the application of hard x-rays offers a nondestructive way to simultaneously probe the magnetization in the surface Fe layer and in the buried SmCo layer. Since both Fe and Sm are ferromagnetic, circularly polarized synchrotron radiation was used. The goal of the experiment was to combine element-specific hysteresis loops and magnetic imaging of both the top Fe and the bottom SmCo layers in order to unequivocally show that the Sm and Fe magnetizations were nearly perpendicularly coupled when the hard SmCo hard layer is demagnetized. This perpendicular coupling of magnetic moments is referred to as biquadratic coupling.

Element-specific remanent hysteresis loops were performed by tuning the energy of the synchrotron radiation to the absorption edges of Fe (7.110 keV) and Sm (6.710 keV). Magnetic contrast was obtained, as in previous examples, by switching the helicity of incident CP photons at each field and measuring the difference in the fluorescence signal. In addition, element-specific imaging of magnetic domains was performed by focusing the circularly polarized x-rays to a spot size of 1 μm by 1 μm. The thickness of both SmCo and Fe layers was 20 nm, and they were grown epitaxially by magnetron sputtering on an MgO substrate. A 20 nm Cr layer was used as a buffer layer between the substrate and the SmCo and a 5 nm Cr layer was a cap. The easy axis was the in-plane c-axis of SmCo.

Fig. 4.2.1 Element-specific hysteresis loops measured at the Sm L_3-edge (6.710 keV) (top) and Fe K-edge (7.110 keV) (bottom). Measurements were done with the field constantly applied (in-field data) and in remanence (field was turned off during data collection).

The experiment involved focusing the beam to a 1x1 $μm^2$ spot size using two mirrors in KB geometry. The mirrors had a Pd coating and were each 10 cm long. The sample was mounted on high-resolution stages (0.07 μm step size) between pole pieces of an electromagnet capable of achieving 0.9 T field strength. The asymmetry (flipping) ratio, which is defined as the contrast in absorption coefficient for opposite helicities of incoming x-rays, was measured in fluorescence geometry using two Ge solid-state
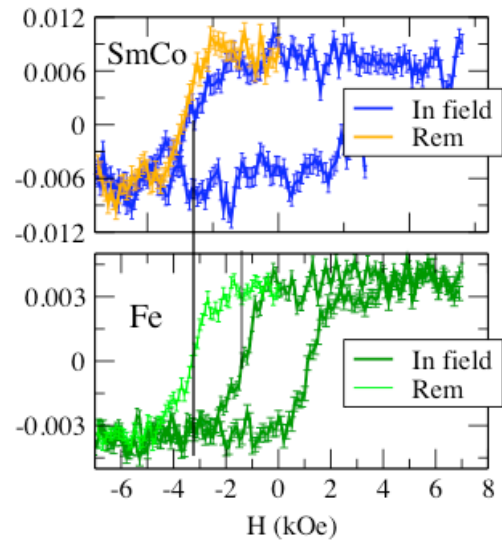
detectors. Circularly polarized x-rays with opposite helicities were generated by phase retarder optics (Hirano, 1993; Lang, 1996) consisting of a single-crystal (111) diamond. Element specific measurements were done at the Fe K edge (7.110 keV) and the Sm L_3 edge (6.710 keV).
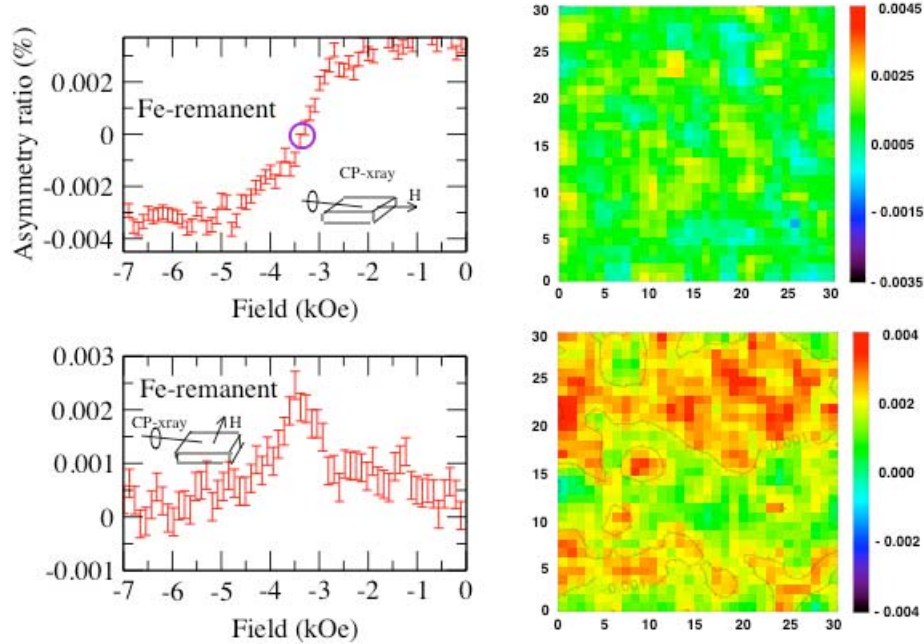

Fig. 4.2.2. Top left: Remanent hysteresis loops performed at the Fe K-edge in geometry where with field (easy axis) and photon helicity directions are parallel. At H_{rem} = –3.4 kOe, the magnetization is zero. Top right: magnetic imaging over a 30 μm x 30 μm area shows no domains structure. Bottom left: Remanent hysteresis loops at the perpendicular geometry peak at H_{rem} = –3.4 kOe, indicating that Fe domains are oriented perpendicular to the easy axis, and thus perpendicular to the Sm domains under the Fe layer. Bottom right: corresponding magnetic imaging clearly shows two large Fe domains, one in red and the other in green.

First, Sm- and Fe-specific hysteresis loops were acquired by measuring the asymmetry ratio at each applied field with the microbeam. Loops taken in-field and in remanence are shown in Fig. 4.2.1. The in-field loops show coercive fields of 3.4 kOe and 1.5 kOe for SmCo and Fe layers, respectively. The remanent hysteresis loops were measured by first fully magnetizing the sample at the saturation field of H = +7 kOe and then applying field H_{rem} before turning the applied field to zero. The Sm-remanent hysteresis indicates the nucleation of oppositely oriented domains at the field strength of H_{rem}=–2.7 kOe. Switching occurs at H_{rem}=–3.4 kOe, where the SmCo layer is demagnetized, i.e., broken into equal number of domains with opposite

orientation. It is plausible that the strong anisotropy of the hard SmCo layer results in the orientation of domains along the easy axis.

Imaging of magnetic domains was subsequently done by scanning the sample in two dimensions with a submicron step size and measuring the asymmetry ratio at each point. An 30x30 μm^2 image taken at the peak of the Sm resonance (6.710 keV), and, at the remanent field of –3.4 kOe, exhibited no domains structure. This means that the domains are either very large or much smaller than the beam size (1 μm^2). The first option can be easily ruled out because the *average* asymmetry ratio corresponds to the zero of the remanent hysteresis loop. A large domain would have resulted in the asymmetry ratio near the extreme parts of the hysteresis loops, either 0.005 or –0.01 as seen in the top part of Fig. 4.2.1. Therefore, the Sm domains are significantly smaller than the probing beam, and, since microbeam illuminates many domains at each pixel the average magnetization is zero.

To determine the structure and orientation of the domains at the top Fe layer, hysteresis loops and magnetic imaging (Fig. 4.2.2) were done at the Fe K edge. While the in-field hysteresis shows that the reversal of Fe domains occurs at H=-1.5 kOe, the remanent hysteresis indicates that the switching occurs at a larger (in absolute value) field of H_{rem}=–2.8 kOe because of the strong interfacial coupling between the Fe and SmCo layers. The reorientation of Fe domains happens at the same field strength as the magnetically hard SmCo layer. The Fe remanent magnetization becomes zero at H_{rem}=–3.4 kOe, where the SmCo underlayer is demagnetized. The zero net magnetization probed with a microbeam could be the consequence of either Fe breaking up into domains oriented along the easy axis that are much smaller than the beam size (similar to Sm domains) or the Fe magnetization is aligned perpendicularly with respect to the applied field and x-ray beam direction. Since XMCD measures the projection of the magnetization along the x-ray helicity (or beam direction), a 90º magnetization direction away from the beam direction would result in the zero asymmetry ratio. The latter scenario could be proved by repeating the measurements in the geometry in which both the sample and magnet are rotated by 90º with respect to photon helicity. In this geometry, the field is still applied along the easy axis, but, if the Fe domains prefer to orient perpendicularly to the easy axis, the projection of the magnetization, and thus the measured asymmetry, would be maximized. This was indeed observed in the Fe remanence loops after rotation: for H_{rem} below –2.5 kOe, the Fe magnetization remained along the easy axis resulting in the zero value of the asymmetry ratio

(Fig. 4.2.2 bottom left). Between -4.5 kOe $<H_{rem}< -2.5$ kOe the Fe magnetization rotates towards a direction perpendicular to the easy axis with a peak corresponding to the zero net magnetization ($H_{rem}=-3.4$ kOe) of the SmCo underlayer. If the H_{rem} field is further decreased, the Fe magnetization direction points again towards the easy axis resulting in the zero XMCD signal. This conclusion was confirmed by imaging. Two images over the 30 μm x 30 μm area were taken at the Fe K edge resonance and in remanence: one with the field (an easy axis) parallel to the photon helicity (top right of Fig. 4.2.2) and the other perpendicular to the photon helicity (bottom panel of Fig. 4.2.2). The absence of domain structure in the parallel geometry indicates that the domains are oriented perpendicular to the easy axis. The possibility of having domains smaller than the beam size and aligned along the easy axis can be dismissed because the acquired image in the perpendicular geometry clearly showed two large (over 10 μm) domains.

In summary, this example demonstrates the utility of combining spectroscopy and microfocusing techniques in the study of heterogeneous magnetic systems. It also shows that the magnetic field can be used which, in turn, opens the possibility of studying domain dynamics.

4.3. Magnetic reversal in antidot arrays

Antidot (hole) arrays in continuous magnetic films have recently received much attention because of their potential advantages over magnetic dot array systems for data storage (Cowburn, 1997). Two advantages are (1) there is no superparamagnetic lower limit to the bit size, and (2) the intrinsic properties of the continuous magnetic film are preserved. Antidot arrays possess unique magnetic properties, such as shape-induced magnetic anisotropy, domain structure, and pinning in laterally confined geometries. Typically, antidot arrays at remanence show three types of domains behaving collectively as a single domain (Toporov, 2000). Domain formation is understood to be mainly the result of the interplay between the intrinsic and shape anisotropy. The coexistence of well-defined domains with individual magnetizations provides an opportunity to study interactions between domains during magnetic switching. Here the XMCD technique is used as a vector magnetometry (VM) to understand the switching mechanism in antidot arrays. The approach is complementary to previous microscopy studies (Toporov, 2000). The results in this example have relevance for future studies of the interlayer coupling under lateral

confinement, because the element-specific XMCD technique is ideally suited for heteromagnetic systems such as Gd/Fe multilayers.

For the VM studies, hysteresis loops were measured by recording XMCD signals. Because XMCD is proportional to the projection of the magnetization vector **M** along the photon momentum direction $\mathbf{k}_{ph}$ near resonance energies [i.e., XMCD is proportional to $\mathbf{k}_{ph}.\mathbf{M} = \cos$. as shown in the inset of Fig. 4.3.1(a)], this technique allows element-specific determination of the orientation of the average magnetization. The technique involves collecting hysteresis curves with more than two orthogonal incident photon directions for a given field (Chakarian, 1995). Multilayer [Fe (3 nm)/Gd (2 nm)]x8 films were prepared on Si substrates by e-beam deposition. Square-shaped

Figure 4.3.1: XMCD magnetic hysteresis loops (circles) measured at the Fe K edge at room temperature. To obtain vector information on the average magnetization, the incident photon beams were rotated with respect to the positive field direction, by = (a) 0°, (b) –45°, (c) –90°, and (d) –135°. The inset in (a) shows a schematic of the experimental setup, where is the angle between the magnetization vector **M** and the incident photon momentum direction $\mathbf{k}_{ph}$, **H** is the applied field, and "EA" and "HA" denote the easy- and hard-axis of the intrinsic anisotropy, respectively. The solid lines represent the calculated hysteresis loops from using micromagnetic simulations.

arrays of circular holes with a period of 2 μm and a diameter of 1 μm were manufactured by using standard lithography and liftoff processes. Magneto-optic Kerr effect (MOKE) hysteresis loops were measured for both unpatterned and patterned films to determine the direction of intrinsic uniaxial magnetic anisotropy. Circularly polarized hard x-rays were produced by a diamond (111) quarter-wave plate operated in Bragg transmission geometry (Lang, 1995). The XMCD effects were measured in fluorescence around the Fe K absorption edge (7.111 keV) by
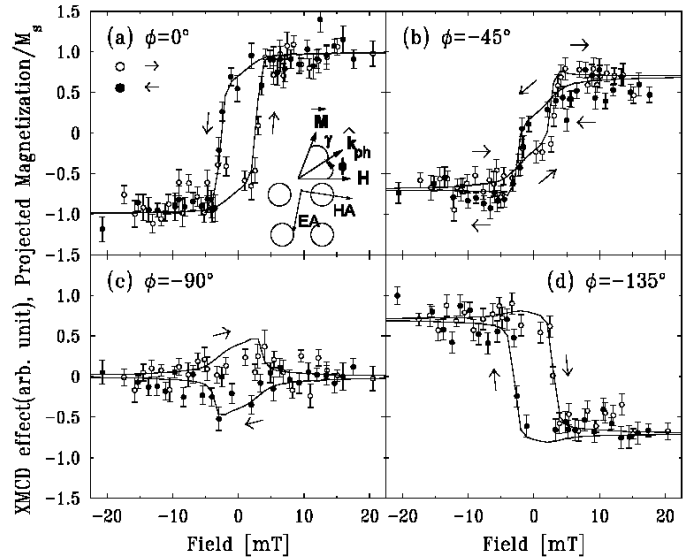
switching the helicity of the incident radiation. For the VM studies, the sample/electromagnet assembly was rotated with respect to the projected incident photon direction.

Figure 4.3.1 shows XMCD hysteresis loops measured with four different directions of incident x-ray beams. ϕ = (a) 0°, (b) -45°, (c) -90°, and (d) –135° with respect to the field applied in the positive direction. While ϕ= 0° corresponds to the conventional hysteresis loop along the applied field direction, the rotation of the average magnetization of the sample at ϕ = -90° can be described by θ_{avg} = -$\tan^{-1}$ (M$_{-90}$/M$_0$). This was surprising because many domains were expected to form. Following this relationship, one can determine a counter-clockwise rotation of magnetization from Fig. 4.3.1(a) and 4.3.1(c) induced by the easy axis orientation of the intrinsic uniaxial anisotropy, as depicted by the inset in Fig. 4.3.1(a). The preferential rotation gives rise to a dramatic asymmetry between the ϕ = -45° and ϕ = -135° loops. Interestingly, ϕ = -45° hysteresis shows three loops whose tie points correspond to

Figure 4.3.2 The spin configurations of antidot arrays obtained from micromagnetic simulations with a sequence of applied fields of (a) 3 mT, (b) 0 mT, and (c) –2 mT. (d) Schematic of the three characteristic domains labeled A, B, and C in the unit cell.

the coercive fields. Since XMCD-VM measures a spatially averaged magnetization, numerical micromagnetic simulations have been performed to reconstruct the microscopic domain configuration. The hysteresis loops were calculated by using micromagnetic simulations and were fitted to the experimental data from XMCD-VM by varying the uniaxial anisotropy, exchange stiffness, and saturation magnetization as parameters. The fitted results from the 2-D code are shown as solid lines in Fig. 4.3.1 and are in good agreement with the measured XMCD hysteresis loops. The reconstructed spin configurations with the best-fit parameters clearly showed three main types of domains, as reported previously (Toporov, 2000).

A sequence of spin configurations reveals that two types of domains rotate coherently while one is pinned (see fig. 4.3.2). To understand intuitively the coherent rotations, we have
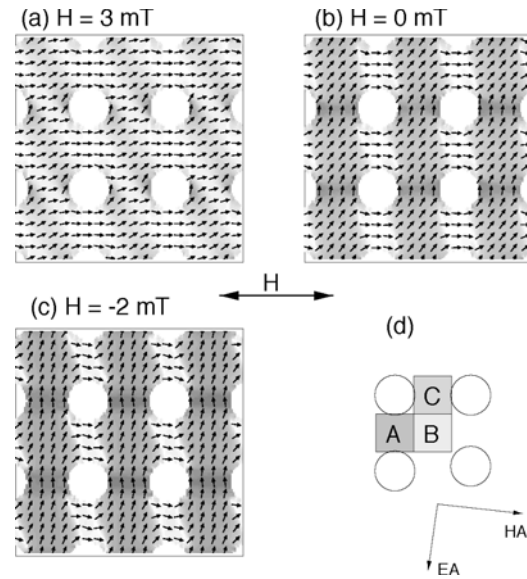
developed a simple phenomenological energy model by employing the Stoner-Wohlfarth single-domain model with an effective shape anisotropy. This model suggests that the interplay between the shape anisotropy and the intrinsic uniaxial anisotropy can explain the coherent rotations of domains, as well as characteristic domain formations in antidot arrays.

This example demonstrates the power of vector magnetometry using XMCD. It may be useful in future applications where one needs to resolve individual contributions to the domain structure in a multicomponent system. The details of this work are given by Lee (2002).

4.4. Inhomogeneous magnetic structures in magnetic multilayers

Inhomogeneous magnetic states, wherein the magnetization direction rotates away from the applied field direction with distance from surfaces and interfaces, are commonly found in a variety of structures. Examples include the spin-flop transitions in giant magneto-resistant (GMR) Fe/Cr multilayers (Wang, 1994), and biquadratic coupling in exchange spring magnet Fe/SmCo bilayers (Vlasko-Vlasov, 2001). Understanding the nature of the interactions leading to these magnetic states is important for tailoring the properties of these and other technologically relevant layered magnetic structures.

Artificial Fe/Gd multilayers are an ideal model system to investigate this question. The markedly different bulk Curie temperatures of Fe (1024K) and Gd (293K), together with strong interlayer antiferromagnetic coupling at the Fe/Gd interface, result in inhomogeneous magnetic depth profiles that depend on surface termination, applied field, and temperature (Camley, 1998). Over a decade ago LePage and Camley (LePage, 1990) predicted that the nucleation site of an inhomogeneous state will either be the surface or the bulk of the multilayer, depending on termination. Termination by the component with the smallest magnetization will lead to surface nucleation wherein the magnetization deviates from the applied field direction only near the surface while the bulk remains field aligned. This inhomogeneous phase has eluded direct experimental detection due to the difficulty in probing surface and bulk states in the same measurement. The challenge is to observe both the existence of a surface-twisted phase and the absence of a bulk twist.

In this example, the penetration depth tunability of x-rays at grazing and larger incidence angles θ_i was exploited to alternately probe surface and bulk magnetic states by XMCD (Haskel, 2003). Figure 4.4.1 shows Gd and Fe hysteresis loops in an Fe-terminated [Fe(35Å)/Gd(50Å)]$_{15}$ /Fe(35Å) multilayer for selected temperatures below, near and above the ferrimagnetic compensation temperature $T_0 \approx 110K$ at which the Fe and Gd magnetizations cancel. For Gd loops, two sets of data are shown corresponding to surface-enhanced loops at $\theta_i =0.43°$ (probes ≈ 2 bilayers) and bulk-sensitive loops at $\theta_i =9.5°$ (probes the whole multilayer). Specular reflectivity data were used to accurately determine the angle used for Gd surface sensitive loops. These loops are obtained from the asymmetry in the absorption coefficient for opposite x-ray helicities at each applied field, $(\mu^+ - \mu^-)/(\mu^+ +\mu^-)$, at resonant energies that maximize the magnetic contrast (Haskel, 2003). Since XMCD measures the projection of the magnetization along the photon wave vector a "flat" loop indicates aligned magnetic states where the Gd(Fe) magnetization is parallel (antiparallel) to the magnetic field H as dictated by their

Figure 4.4.1. Gd (left) and Fe (right) hysteresis loops. The "flat" loops correspond to Gd dominant (10K) and Fe dominant (200K) field-aligned configurations. The "tilted" loops correspond to magnetic twisted configurations where the magnetization deviates from the applied field direction in the surface alone (70, 90K) or also in the bulk (110K). Solid lines are obtained from Landau-Lifshitz calculations of the magnetization profiles.

AFM exchange coupling. A "tilted" loop, however, indicates a reduced projection due to canting of the moments away from H. This canting, which increases with H, can only be driven by a
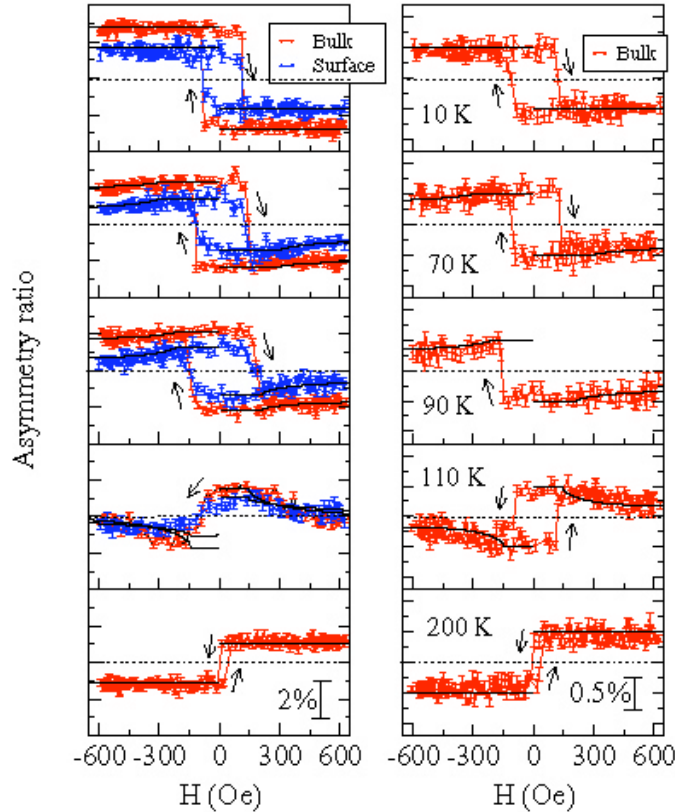
reduction in Zeeman energy, since exchange is already minimized in the aligned geometry. A gain in the net magnetization has to take place for a twist to occur. Since the magnetization of Gd is larger than that of Fe below T_0, this can only be achieved if the Fe sublattice twists more toward the applied field than the Gd sublattice twists away from it, in order to compensate for the increased Zeeman energy of the latter. These different twist angles, however, increase the exchange energy. The competition between this increased exchange energy and the reduction in Zeeman energy determines the magnetic configuration.

At 10K the Gd layers dominate the Zeeman energy and align with H, while Fe is constrained antiparallel by AF exchange. Here a twisted phase would require an applied field outside the experimental range. At 70 and 90 K, "tilted" Gd loops are measured in the top part of the multilayer, while bulk-sensitive Gd loops show less tilting, indicating larger canting of the moments at the surface. The decrease in Gd magnetization with T, as seen from the reduced edge jump, decreases the required field for nucleation of a twist to within the experimental range. At 90K the Gd surface-sensitive XMCD is reduced by 65% at H=600 Oe, while the bulk XMCD decreases only by 20%. Considering the probing depth of ≈ 2 bilayers at $\theta_i=0.43°$ and, given that top and bottom parts of the multilayer are equivalent, the average reduced magnetization m in the inner 11 bilayers can be obtained from [0.35× 4 + 11× m]/15=0.8. This yields m=0.96; i.e., the interior of the multilayer remains mostly field aligned. The reduction in the bulk Gd loops at 70 and 90K is mainly due to the surface contribution. At 110K, the tilting or twist already propagates throughout the multilayer, as evidenced from the now significantly tilted surface and bulk loops. A correlated reversal in the sign of Gd and Fe loops at this temperature shows that Fe now dominates the Zeeman energy contribution. At 200K the loops are again "flat", with the Fe aligning along the field and Gd antiparallel.

Figure 4.4.2 also shows theoretical calculations of the static magnetization profile. The surface nucleation of the inhomogeneous state is clearly observed. To compare with the experimental data, the calculated magnetization depth profiles were weighted, each element separately, to account for the depth selectivity of our XMCD measurements at the different incidence angles. The results of this averaging are shown by the solid lines on the loops, where the agreement with experiment supports the conclusion of the extent of the penetration depth at nucleation of ≈ 200 Å (2-3 bilayers). The energy barrier for a twist of the minority sublattice (Fe) towards the applied field direction H is decreased at the surface due to the absence of Fe/Gd

interlayer exchange coupling at the terminal Fe layers. This results in surface nucleation of the inhomogeneous state while, the increased exchange energy cost in the bulk does not allow the twist to penetrate past the first few Fe/Gd bilayers.
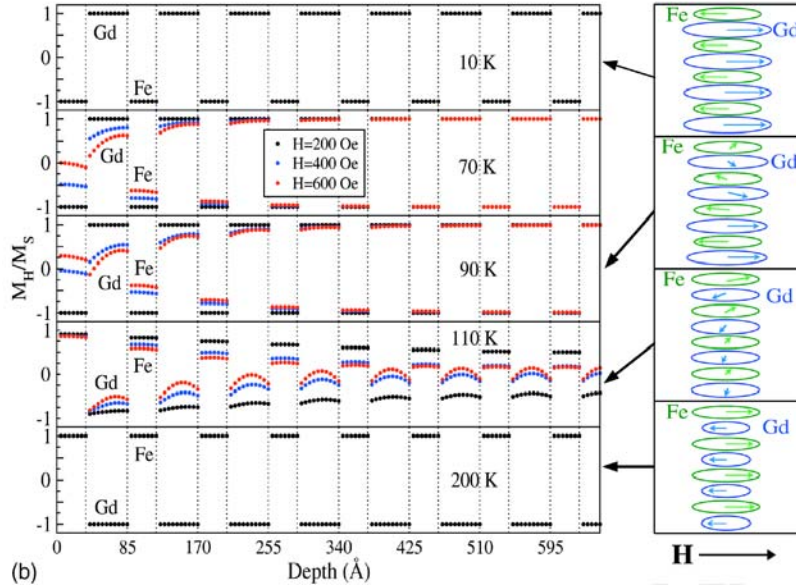

Figure 4.4.2. Theoretical magnetization profiles for half of the multilayer structure (other half mirror symmetric). Magnetization is normalized to saturation value at each temperature. Schematic diagram (right) represents the magnetization (intralayer averaged) in the upper four bilayers at the different temperatures and H=600 Oe.

In summary, surface nucleation of a twisted magnetic state when the a Gd/Fe multilayer is terminated by the minority (Fe) component was observed. The surface state penetrates $\approx$ 200 Å into the bulk due to strong interlayer coupling at Fe/Gd interfaces. These results are the first direct confirmation of the long-ago predicted inhomogeneous magnetic phase in the strongly coupled model system. Furthermore, this method opens a way towards distinguishing surface from bulk states in inhomogeneous magnetic systems.

5.   CONCLUSIONS AND OUTLOOK

In the past several years, the application of synchrotron techniques to the study of magnetic nanostructures has emerged as a viable and complementary tool to the more conventional techniques described in this book. Examples in this chapter are meant to illustrate some of the advantages that diffraction, reflectivity and spectroscopy techniques could offer. We particularly want to emphasize that the penetration ability of hard x-rays enables nondestructive study of buried structures and interfaces. We hope that this feature, coupled with the high brightness of third-generation synchrotron sources, energy selectivity, high momentum resolution and well-defined polarization characteristics will entice practitioners to consider synchrotron radiation techniques for resolving problems in nanomagnetism.

References

D.D. Awschalom, M.E. Flatté, and N. Samarth, *Scientific American*, p. 68, June (2002)

D.H. Bilderback, S.A. Hoffman and D.J. Thiele, *Science* **263**, 201 (1994).

M. Blume, *J.Appl.Phys.* **57**, 3615 (1985).

M. Blume and D. Gibbs, *Phys. Rev. B* **37**, 1779 (1988).

M. Blume in *Resonant Anomolous X-Ray Scattering – Theory and Practice*, 495 (1994), Elsevier Science.

R. E. Camley and D. R. Tilley, *Phys. Rev. B* **37**, 3413 (1988)

R. E. Camley*, Phys. Rev. B* **39**, 12316 (1989).

P. Carra , B.T. Thole, M. Altarelli and X. Wang, *Phys. Rev.Lett.* **70**, 649 (1993).

R.J. Celotta, J. Unguris, M.H. Kelley, and D.T. Pierce, "Techniques to measure magnetic domain structures", in *Methods in Materials Research: Current Protocols*, edited by E. Kaufmann, Ch. 6b.3 (John Wiley & Sons, New York, 2001).

V. Chakarian, Y.U. Idzerda, G. Meigs, *et al., Appl. Phys. Lett.* **66**, 3368 (1995).

J. Chavanne and P. Elleaume, *Undulators, Wigglers and Their Applications*" edited by H. Onuki
and P. Elleaume, Taylor & Francis, London, 2003.

C.T. Chen, F. Sette, Y. Ma, *et al., Phys. Rev. B* **43**, 7262 (1990).

C.T. Chen, Y.U. Idzerda, H.-J. Lin, *et al., Phys. Rev. Lett.* **75**, 152 (1995).

R.P. Cowburn, A.O. Adeyeye, and J.A.C. Bland, *Appl. Phys. Lett.* **70**, 2309 (1997).

R.J. Dejus, I.B. Vasserman, S. Sasaki and E.R. Moog, ANL/APS/TB-45 (2002).

J. W. Freeland, V. Chakarian, K. Bussmann *et al., J. Appl. Phys.* **83**, 6290 (1998).

E. F. Fullerton, J. S. Jiang, C. Rehm, C. H. Sowers, S. D. Bader, J. B. Patel, and X. Z. Wu, *Appl. Phys. Lett.* **71**, 1579 (1997).

E. F. Fullerton, J. S. Jiang, M. Grimsditch, C. H. Sowers, and S. D. Bader, *Phys. Rev. B* **58**, 12193 (1998).

D. Gibbs, D.E. Moncton, K.L. D'Amico *et al., Phys. Rev Lett* **55**, 234 (1985).

D. Gibbs, D.R. Harshman, E.D. Isaacs *et al., Phys. Rev. Lett.* **61**, 1241 (1988).

D. Gibbs, G. Grübel, D.R. Harshman, *et al., Phys. Rev.B* **45**, 5663 (1991).

D. Givord et al., *Solid State Commun.* **51**, 857 (1984).

J.P. Hannon, G.T. Tramell, M. Blume and D. Gibbs, *Phys. Rev. Lett.* **61** 1245 (1988).

D. Haskel, G. Srajer, J.C. Lang, *et al., Phys. Rev. Lett.* **87**, 207201 (2001).

D. Haskel, G. Srajer, Y. Choi, *et al., Phys. Rev.* **B 67**, 180406 (2003).

D. Haskel et al., IEEE Trans. Mag. (accepted, 2004);

J. F. Herbst, *Rev. Mod. Phys.* **63**, 819 (1991).

J.P. Hill and D.F. McMorrow, *Acta Cryst.* **A52**, 236 (1996).

K. Hirano, T. Ishikawa, and S. Kikuta, *Nucl. Instrum. Methods* **A336**, 343 (1993).

S.K-Kim and J. B. Kortright, *Phys. Rev. Lett.* **86**, 347 (2001).

G. van Der Laan, B.T. Thole, G.A. Sawatzky, J.B. Geodkoop, J.C. Fluggle, J.M. Esteva, R. Karnatak, J.P. Remeika and H.A. Dabkowska, *Phys. Rev. B* **34,** 6529 (1986).

J.C. Lang and G. Srajer, *Rev. Sci. Instrum.* **66**, 1540 (1995).

J.C. Lang, G. Srajer, and R.J. Dejus, *Rev. Sci. Instrum.* **67**, 62 (1996).

J.C. Lang, J. Pollmann, D. Haskel, G. Srajer, J. Maser, J. S. Jiang, S. D. Bader, SPIE Proc. **4499**, 1 (2001).

J.C. Lang, D.R. Lee, D. Haskel, *et al., J. Appl. Phys.* **95**, 1 (2004).

D.R. Lee, Y. Choi, C.Y. You, *et al., Appl. Phys. Lett.* **81**, 4997 (2002).

D.R. Lee, S.K. Sinha , D. Haskel, *et al.,* Phys. Rev. **B 68**, 224409 (2003a).

D.R. Lee, S.K. Sinha, C.S. Nelson, *et al.,* Phys. Rev. **B 68**, 224410 (2003b).

J.G. LePage and E.E. Camley, *Phys. Rev. Lett.* **65**, 1152 (1990).

D.F. McMorrow, D. Gibbs and J. Bohr, *Handbook on the Physics and Chemistry of Rare Earths,* Volume 26, 1 (1999) Elsevier Science

K. Namikawa, M. Ando, T. Nakajima and H. Kawata, *J.Phys.Soc.Jpn.* **54**, 4099 (1985).

C. S. Nelson, G. Srajer, J.C. Lang, *et al.*, *Phys. Rev.* **B 60**, 12234-12238 (1999).

R. M. Osgood III, S.K. Sinha, J.W. Freeland, *et al.*, *J. Magn. Magn. Mater.* **198-199**, 698 (1999).

F. Pfeiffer, C. David, M. Burghamer *et al., Science* **297**, 230 (2002).

J. Pollmann, G. Srajer, J. Maser, J.C. Lang, C. S. Nelson, C. T. Venkataraman, and E. D. Isaacs, *Rev. Sci. Instrum.* **71**, 2386 (2000).

J. Pollmann, G. Srajer, D. Haskel, *et al., J. Appl. Phys.* **89**, 7165-7167 (2001).

R. Schad *et al., Europhysics Letters* 44, 379 (1998)

A. Scholl, J. Stöhr, J. Lüning, *et al., Science* **287**, 1014 (2000).

G. Schütz, W. Wagner, W. Wilhelm *et al., Phys.Rev.Lett* **58**, 737 (1987).

G. Schutz, R. Frahm, P. Mautner, *et al., Phys. Rev. Lett*. **62**, 2620 (1989).

S. K. Sinha *et al., Phys. Rev. B* **38**, 2297 (1988)

J. Stöhr, H. A. Padmore, S. Anders *et al., Surface Rev. and Lett.* **6**, 1297 (1998).

C. Sutter, G. Grübel, C. Vettier, F. de Bergevin, A. Stunault, D. Gibbs and C. Giles, *Phys. Rev B* **55**, 954 (1997).

M. Taborelli *et al., Phys. Rev. Lett.* **56**, 2869 (1986).

H. Takano, Y. Suzuki and A. Takeuchi, *Jpn.J.Appl.Phys.* **42**, L132 (2003).

B. T. Thole, P. Carra, F. Sette and G. van der Laan, *Phys.Rev.Lett.* **68**, 1943 (1992).

A.Y. Toporov, R.M. Langford, and A.K. Petford- Long, *Appl. Phys. Lett.* **77**, 3063-3065 (2000).

V.K. Vlasko-Vlasov, U. Welp, J.S. Jiang, D.J. Miller, G.W. Crabtree, and S.D. Bader, *Phys. Rev. Lett*. **86**, 4386 (2001).

R. W. Wang *et al., Phys. Rev. Lett.* **72**, 920 (1994)

W. Yun, B. Lai, Z. Cai *et al.,Rev.Sci.Instrum.* **70**, 2238 (1999).